

Comparison of Bar Formation Mechanisms. IIIA. The role of classical bulges in spontaneous bar formation

YIRUI ZHENG,^{1,2,3,4,5} JUNTAI SHEN,^{3,4,5} AND BIN-HUI CHEN^{6,3,4}

¹*School of Physics and Astronomy, Anqing Normal University, Anqing 246011, P.R. China*

²*Institute of Astronomy and Astrophysics, Anqing Normal University, Anqing 246133, P.R. China*

³*Department of Astronomy, School of Physics and Astronomy, Shanghai Jiao Tong University, 800 Dongchuan Road, Shanghai 200240, P.R. China, jtshen@sjtu.edu.cn*

⁴*State Key Laboratory of Dark Matter Physics, School of Physics and Astronomy, Shanghai Jiao Tong University, Shanghai 200240, P.R. China*

⁵*Key Laboratory for Particle Astrophysics and Cosmology (MOE) / Shanghai Key Laboratory for Particle Physics and Cosmology, Shanghai 200240, P.R. China*

⁶*Tsung-Dao Lee Institute, Shanghai Jiao Tong University, Shanghai 200240, P.R. China*

ABSTRACT

We run a suite of N -body simulations to investigate how classical bulges affect bar formation and properties under the internal formation mechanism. We incorporate bulges of varying mass and compactness into disk galaxy models and evolve them in isolation to examine the resulting bar pattern speeds and growth timescales. A more massive/compact bulge increases the Toomre Q stability parameter and the circular velocity in the central region, while decreasing the disk mass fraction. It therefore delays the onset of bar formation and increases the bar growth timescale; sufficiently strong bulges can suppress bar formation entirely. During the formation stage, bars exhibit higher initial pattern speeds and faster deceleration rates when the bulges become more massive or compact. This faster deceleration persists after the bar buckling phase, leading to slower-rotating bars in the secular growth stage. However, when the bulge’s “diluting” effect on the measured bar strength is removed or reduced, all bars within the same disk share similar distributions in the pattern speed–bar strength (Ω_p – A_2) space during the secular growth stage. They also show comparable ratios of the co-rotation radius to the bar length ($\mathcal{R} = R_{\text{CR}}/R_{\text{bar}}$) in this stage. These results suggest that the bulge’s influence on the pattern speed is more significant during the bar formation stage, while in the secular growth stage, the bulge’s effect may be less important, and the disk component dominates the pattern speed evolution.

Keywords: galaxies: kinematics and dynamics — galaxies: structures

1. INTRODUCTION

Galactic bars are common and important structures of spiral galaxies. In the local universe, optical surveys find bars in nearly 50% of disk galaxies, a fraction that rises to approximately two-thirds in infrared bands (Marinova & Jogee 2007; Menéndez-Delmestre et al. 2007; Erwin 2018; Lee et al. 2019). Although less frequent at higher redshifts, bars are still present, constituting roughly 13% of galaxies at $2 < z \leq 3$ (Le Conte et al. 2024) and have been detected as early as $z \sim 4$ (Guo et al. 2024). These

structures play an important role in driving the evolution of their host galaxies by fueling gas inflows, regulating star formation, and contributing to the formation of pseudo-bulges (Masters et al. 2011; Li et al. 2015; Lin et al. 2017, 2020; Iles et al. 2022). Given their ubiquity and influence, understanding the formation and evolution of bars is critical in galactic dynamics.

Galactic bars can form via two primary mechanisms: internal instability and external perturbations. The internal, or spontaneous, mechanism arises from gravitational instability within the disk itself (Hohl 1971; Ostriker & Peebles 1973; Sellwood 2014; Lokas 2019a). A well-established mechanism for spontaneous bar formation is the swing amplification feedback loop that was

first introduced by Goldreich & Lynden-Bell (1965) and Julian & Toomre (1966), later elaborated in detail by Toomre (1981), and more recently revisited and clarified by Binney (2020). However, the presence of a strong bulge or central mass concentration can introduce inner Lindblad resonances (ILR), which disrupts this feedback loop and thereby suppresses bar formation (Toomre 1981; Binney & Tremaine 2008). If not disrupted, the feedback loop predicts an exponential growth in bar strength.

The growth rate, or equivalently, the formation timescale of bars formed via internal instability, is found to be influenced by several factors, including the bulge-to-disk mass ratio (Kataria & Das 2018), the Toomre Q parameter (Hozumi 2022; Worrakitpoonpon 2025), and the disk thickness (Ghosh et al. 2023). Fujii et al. (2018) reported an exponential decrease in formation timescale with increasing disk mass fraction—the “Fujii relation”—later confirmed by Bland-Hawthorn et al. (2023). The latter study introduced a key methodological improvement: it quantified the exponential growth timescale predicted by the swing amplification loop to measure bar formation instead of using the time the bar strength exceeds a fixed threshold (e.g., $A_{2,max} > 0.2$). Chen & Shen (2025) extended the Fujii relation in disk galaxies to a three-dimensional parameter space of disk mass fraction, Toomre Q , and disk thickness. Their empirical relation revealed a linear dependence of the bar growth timescale on both Q and the disk thickness.

The disk mass fraction is established as the key factor governing the bar formation timescale (Fujii et al. 2018; Bland-Hawthorn et al. 2023, 2024, 2025; Chen & Shen 2025). Since the presence of a bulge reduces this fraction, the bulge component is consequently expected to have a significant effect on the timescale for bar formation. In addition, bulges increase the Toomre Q parameter, particularly in the inner disk, and may also influence the disk thickness. Therefore, bulges can affect bar formation through these two additional factors as well.

Several studies have examined how bulges or central mass concentrations (CMCs) suppress bar formation, although a universal, quantitative criterion for suppression remains elusive due to the problem’s inherent complexity (e.g., Kataria & Das 2018; Saha & Elmegreen 2018; Jang & Kim 2023; Worrakitpoonpon 2025). Nonetheless, consistent trends regarding the bulge’s influence on bar properties have emerged. Kataria & Das (2018) demonstrated that bars have higher pattern speeds in galaxies with more massive bulges, and that the pattern speed decelerates more rapidly as the bulge mass fraction increases. Jang &

Kim (2023) confirmed that bars tend to be stronger, longer, and rotate more slowly in galaxies with less massive and less compact bulges. This trend is further supported by McClure et al. (2025), who also validated it observationally in a sample of 210 MaNGA disk galaxies, finding that slow bars are preferentially associated with weaker bulges.

Besides internal instabilities, bars can also be triggered by external perturbations, such as tidal forces from galaxy clusters, flyby encounters, collisions, or mergers (Byrd et al. 1986; Gauthier et al. 2006; Lokas et al. 2016; Martinez-Valpuesta et al. 2017; Lokas 2019b). In this series of papers, we aim to comprehensively compare the properties of bars formed via internal instability versus those formed under external perturbations.

In the first paper of this series (Zheng & Shen 2025, Paper I hereafter), we conducted a suite of controlled N -body simulations in which bars form either internally or under tidal perturbations. We constructed three pure disk galaxy models of varying dynamical “hotness” and simulated their evolution both in isolation and under flyby interaction. We then measured bar properties, comparing pattern speeds in Paper I and extended the comparison to exponential growth rates in the second paper (Zheng et al. 2025, Paper II hereafter). For cold and warm disks—which can form bars spontaneously in isolation—tidal interactions promote bars to a more advanced evolutionary stage. Nevertheless, these tidally induced bars exhibit pattern speeds and growth timescales similar to their spontaneously formed counterparts within the same disk. In hot disks, which are stable against internal bar instability, a bar forms only under external perturbations and rotates more slowly than bars in cold or warm disks. Therefore, if “tidally induced bars” refer exclusively to those in otherwise bar-stable galaxies, they do rotate more slowly. However, this difference is attributed to the intrinsic properties of the host galaxy rather than to the formation mechanism itself. As for growth timescales of these bars, their growth deviates from an exponential profile and is better described by a linear function, which may suggest that these tidally forced bars do not adhere to the swing amplification mechanism.

The third objective of this paper series is to investigate how classical bulges influence bar formation and properties. In the present work (Paper IIIA), we focus on their effects under the *internal* formation mechanism. The upcoming companion study (Paper IIIB) will extend this investigation to the *external* formation scenario, examining whether the influence of bulges differs between bars formed via these two distinct mechanisms.

Paper IIIA is organized as follows. In Section 2, we describe the construction of galaxy models with varying bulge properties. Section 3 investigates the influence of classical bulges on the pattern speed of spontaneously formed bars. In Section 4, we perform an exponential fit to the bar growth to quantify how bulge properties affect the bar growth timescale and onset time. Finally, we summarize our findings in Section 5.

2. SIMULATIONS

2.1. Galaxy models

In Paper I and Paper II, we employ a suite of pure-disk models generated with the AGAMA software (Vasiliev 2019). These models share a common density profile but differ only in the velocity dispersion of their stellar disks. They comprise two components: an exponential, quasi-isothermal stellar disk and a truncated Hernquist dark matter (DM) halo. The stellar disk has a mass of $M_* = 3.6 \times 10^{10} M_\odot$, a scale length of $R_d = 2$ kpc, and a scale height of $h_z = 0.4$ kpc. The DM halo is characterized a mass of $M_{\text{halo}} = 3.6 \times 10^{11} M_\odot$ and a scale radius of $a = 13.7$ kpc. For comprehensive details on both components, we refer the reader to Paper I.

In this study, we further incorporate a classical bulge component into the galaxy model. Its density distribution is given by a truncated Hernquist profile (Hernquist 1990):

$$\rho_b = \frac{M_b}{2\pi} \frac{r_b}{r(r+r_b)^3} \times \exp[-(r_b/r_{\text{cut},b})^2]. \quad (1)$$

Here, the density profile consists of the standard Hernquist form—parameterized by the total mass M_b and the scale radius r_b —multiplied by an exponential cutoff term. This cutoff, governed by the cutoff radius $r_{\text{cut},b}$, acts to suppress the density at large radii. In all models, we set $r_{\text{cut},b} = 8 r_b$.

To create models with varying bulge prominence, we consider a range of bulge-to-disk mass ratios: $B/D = 0.1, 0.2, \text{ and } 0.3$. This yields bulge masses of $M_b = 3.6 \times 10^9 M_\odot, 7.2 \times 10^9 M_\odot, \text{ and } 1.08 \times 10^{10} M_\odot$, respectively. Similarly, we explore different bulge compactness by varying the ratio of the bulge scale radius to the disk scale length, $r_b/R_d = 0.2, 0.4, 0.6$, with smaller values indicating a more compact bulge. The corresponding bulge scale radii are $r_b = 0.4$ kpc, 0.8 kpc, and 1.2 kpc, respectively.

The stellar disk velocity distribution in AGAMA is set by an action-based distribution function (DF). The key stability parameter from the DF is the radial velocity dispersion, which declines exponentially with a scale length $R_{\sigma,R} = 2 R_d$. We define three model series—cold, warm, and hot disks—by setting the central radial

velocity dispersion to $\sigma_{R,0} = 73$ km/s, 124 km/s, and 226 km/s, respectively. Each series comprises one pure disk model and nine galaxy models with bulges (varying in mass and compactness) as described previously.

We quantify the stability of the stellar disk by the Toomre Q parameter, which is defined as:

$$Q = \frac{\kappa \sigma_R}{3.36 G \Sigma}, \quad (2)$$

with κ , σ_R , G , and Σ representing the epicycle frequency, radial velocity dispersion, gravitational constant, and disk surface density, respectively. The top row of Figure 1 shows the Q profiles for the cold model series. Relative to the pure disk case, Q is similar in the outer disk but exhibits a substantial increase in the inner region. This increase is particularly pronounced for more massive (larger B/D) and more compact (smaller r_b/R_d) bulges.

The middle row of Figure 1 presents the circular speed curves $v_c(R)$ for the cold series, along with decompositions into contributions from the halo, stellar disk, and bulge components. The circular speed increases with bulge mass, particularly in the inner region. Furthermore, the inner profile of $v_c(R)$ is significantly modified by the presence of a compact bulge.

Following Fujii et al. (2018) and Bland-Hawthorn et al. (2023), we compute the f_{disk} parameter as the mass ratio of the disk to the total galaxy:

$$f_{\text{disk}}(R) = \frac{v_{c,\text{disk}}^2(R)}{v_{c,\text{total}}^2(R)}. \quad (3)$$

This parameter is shown in the bottom row of Figure 1; the legends indicate its value at $R = 2.2 R_d$, the radius where the rotation curve typically peaks, and which is used in the Fujii relation. The bulge component reduces f_{disk} as anticipated, with more massive bulges producing lower values. In contrast, bulge compactness significantly affects f_{disk} only in the innermost region, whereas it exerts limited influence on f_{disk} at $2.2 R_d$.

The results for the warm and hot model series follow the same trend and are therefore omitted for brevity.

2.2. Simulation details

To study the influence of the bulge on spontaneous bar formation, each galaxy model is simulated in isolation for 6 Gyr with GADGET-4 (Springel 2005; Springel et al. 2021). The particle numbers are as follows: one million for the DM halo, 0.5 million for the stellar disk, and $0.5 \times (B/D)$ million for the bulge. This corresponds to particle masses of $3.6 \times 10^5 M_\odot$ for the halo and $7.2 \times 10^4 M_\odot$ for the stellar components. The gravitational softening lengths are 57 pc for DM particles and 23 pc for stars.

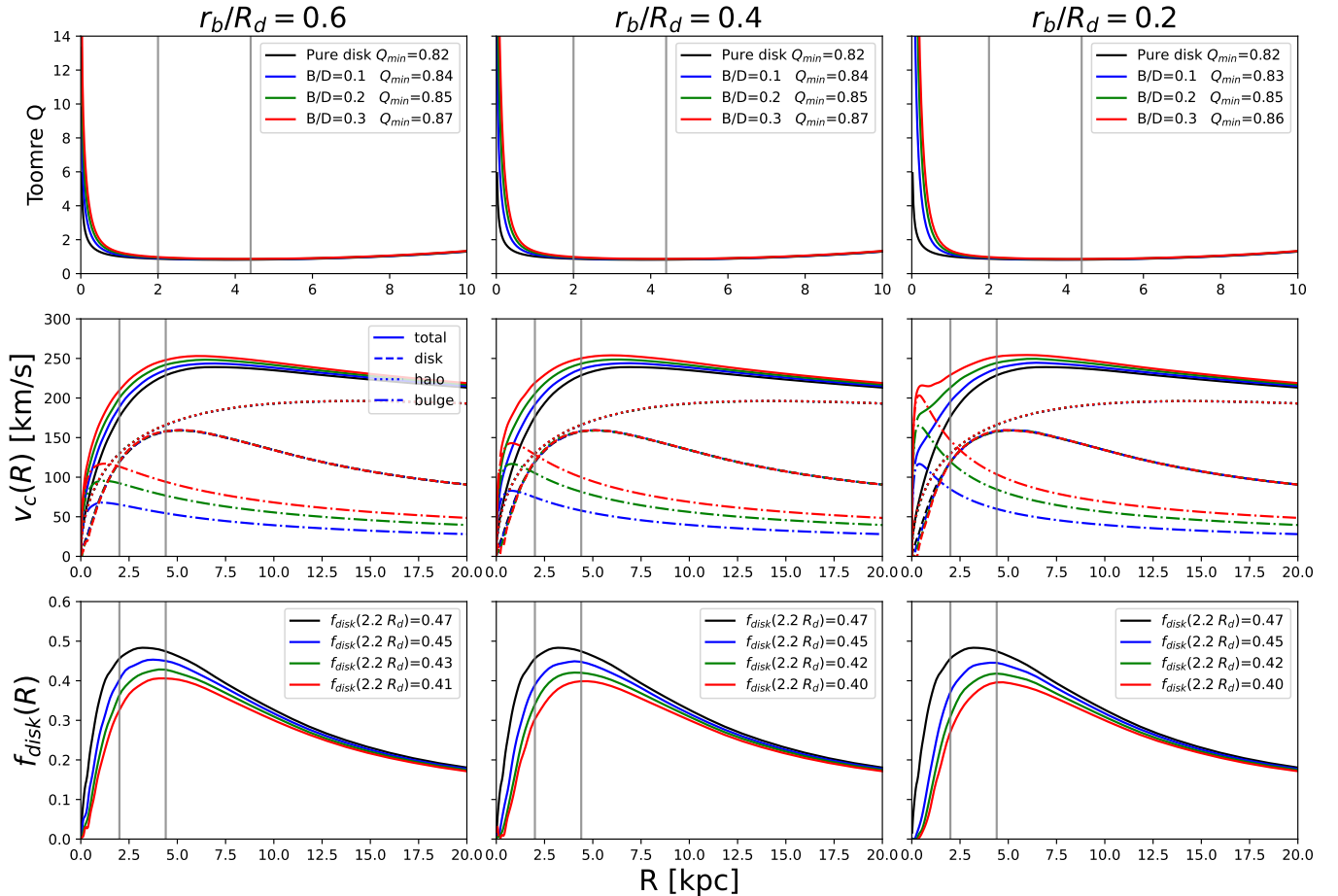


Figure 1. Toomre Q profiles (top row), circular speeds (middle row), and disk mass fraction f_{disk} (bottom row) for the cold series models. Columns show increasing bulge compactness (left to right), with the scale radius (length) ratio $r_b/R_d = 0.6, 0.4,$ and 0.2 . Solid lines trace models of varying bulge-to-disk mass ratio (B/D), with the minimum Q value and $f_{\text{disk}}(2.2 R_d)$ noted in the legend. The middle row decomposes $v_c(R)$ into contributions from bulge (dash-dotted), stellar disk (dashed), and DM halo (dotted) components. Vertical gray lines indicate $1R_d$ and $2.2R_d$ (where $R_d = 2$ kpc).

Although the mass resolution in our simulations is moderate, it is adequate for tracking bar growth. This is supported by the findings of [Dubinski et al. \(2009\)](#), who demonstrated convergence in key aspects of bar evolution (such as growth, pattern speed, dark matter halo density profile, and nonlinear orbital resonance analysis) when comparing simulations with one million to ten million halo particles.

3. BULGE EFFECTS ON BAR PATTERN SPEED

3.1. Bar strength and pattern speed

Bar strength A_2 and pattern speed Ω_p are quantified via Fourier analysis. We compute the $m = 2$ Fourier coefficients within a cylindrical radius $R \leq 4R_d$ (i.e.,

$R \leq 8$ kpc for our models):

$$a_2 = \frac{\sum_{i=1}^N m_i \cos(2\phi_i)}{\sum_{i=1}^N m_i}, \quad (4a)$$

$$b_2 = \frac{\sum_{i=1}^N m_i \sin(2\phi_i)}{\sum_{i=1}^N m_i}, \quad (4b)$$

summing over particles with mass m_i and azimuth angle ϕ_i . The bar strength A_2 is then decided as:

$$A_2 = \sqrt{a_2^2 + b_2^2}, \quad (5)$$

while the position angle of the bar ϕ_{bar} is :

$$\phi_{\text{bar}} = \frac{1}{2} \arctan(b_2/a_2). \quad (6)$$

The pattern speed Ω_p is defined as the time derivative of the position angle, i.e.,

$$\Omega_p = \Delta\phi_{\text{bar}}/\Delta t. \quad (7)$$

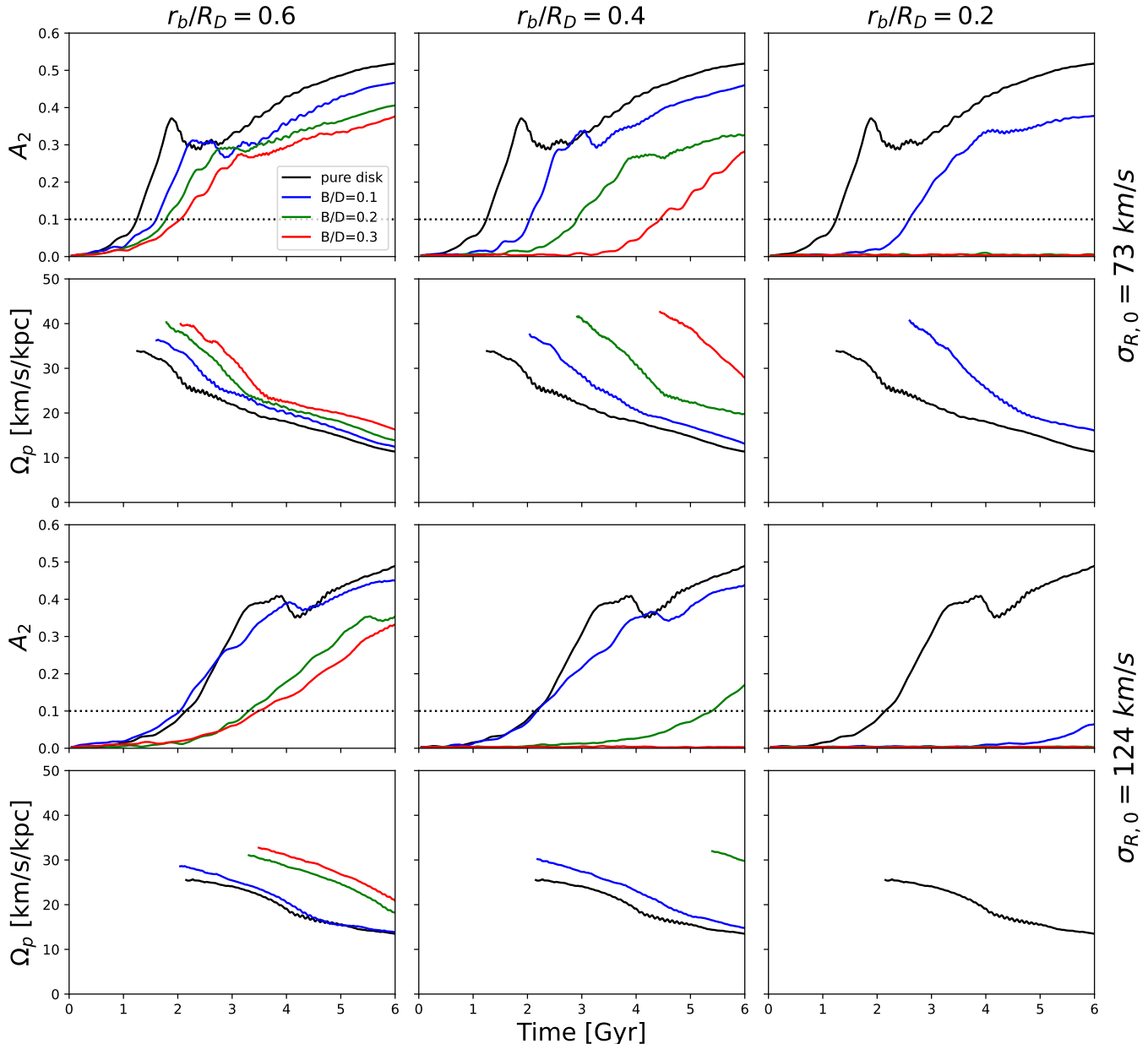


Figure 2. Bar strength A_2 (odd rows) and pattern speed Ω_p (even rows) for different models. Models are arranged by increasing bulge compactness from left to right, with $r_b/R_d = 0.6, 0.4,$ and 0.2 . Rows show results of different dynamical hotness: the cold series ($\sigma_{R,0} = 73$ km/s, top two rows) and the warm series ($\sigma_{R,0} = 124$ km/s, bottom two rows). The results for the hot series ($\sigma_{R,0} = 226$ km/s) are not shown as no bar forms in isolation for any of the models in this series.

We measure Ω_p only when $A_2 \geq 0.1$, since ϕ_{bar} is not well-defined during the early stages of bar formation.

Figure 2 shows the evolution of bar strength A_2 and pattern speed Ω_p for our models during the isolated simulations. The raw A_2 and Ω_p data may fluctuate due to transient features such as spurs or spiral arms attached at the ends of the bars. We therefore smooth both quantities with a 0.2 Gyr moving-average window to mitigate these fluctuations.

Results for the cold model series ($\sigma_{R,0} = 73$ km/s) are displayed in the top two rows. A bulge component delays bar formation compared to the pure disk model, which will be further quantified in Section 4. At a given bulge mass (B/D), greater compactness (smaller r_b/R_d) results in a longer bar formation delay. These trends align with the increased disk stability (higher Toomre Q) in the inner region caused by a stronger bulge, as seen in Figure 1. Moreover, for sufficiently massive ($B/D \geq 0.2$) and compact ($r_b/R_d = 0.2$) bulges, bar

formation is completely suppressed over the full 6 Gyr simulation. The suppression is physically anticipated. As demonstrated in Figure 1, a strong bulge elevates the central circular speed and thereby the angular frequency. This may establish an inner Lindblad resonance (ILR), which prevents density waves from propagating and thus breaks the swing amplification feedback loop. Consequently, bar formation is suppressed.

We find that bars formed in models with more massive or compact bulges have higher pattern speeds at birth. This is consistent with the higher circular speed (and thus higher angular speed) in the inner regions of such models, as seen in Figure 1. Our finding is in agreement with several previous studies (Kataria & Das 2018; Jang & Kim 2023; McClure et al. 2025), which similarly observed faster pattern speeds for bars in galaxies with more prominent bulges.

After their formation, bars undergo gradual deceleration—a well-established result commonly seen in the literature (Weinberg 1985; Debattista & Sellwood 2000; Athanassoula 2003) and in our own previous work (Paper I). This deceleration is driven by the capture of disk stars onto the outer parts of the bar and by the dynamical friction between the bar and the dark matter halo. Bars formed in models with a more massive or compact bulge decelerate faster after formation, as indicated by the steeper gradient in their Ω_p evolution. This finding is consistent with Kataria & Das (2018). The differences in bar pattern speed and deceleration rate are more clearly identified in the pattern speed–bar strength ($\Omega_p - A_2$) space. This phase-space representation accounts for the different evolutionary stages of bars and will be explored in Section 3.2.

The bottom two rows of Figure 2 show results for the warm model series ($\sigma_{R,0} = 124$ km/s). The presence of a bulge component similarly delays bar formation and raises the pattern speed at formation. More models in this series fail to form a bar within 6 Gyr; the warmer disk is intrinsically less susceptible to the bar instability, and the bulge provides additional stabilization. For high bulge compactness ($r_b/R_d = 0.2$), even a low-mass bulge ($B/D = 0.1$) suffices to suppress the formation of identifiable bars ($A_2 \geq 0.1$) within 6 Gyr.

We omit the results for the hot model series, as none of these models form a spontaneous bar within 6 Gyr. The hot stellar disk is intrinsically stable against bar formation, as demonstrated in Paper I, and the addition of a bulge further stabilizes the system. Consequently, the hot series models are excluded from the subsequent analysis in this paper.

3.2. Pattern speed–bar strength ($\Omega_p - A_2$) space

In Paper I, we found that tidally induced bars in the cold and warm disks can appear to have lower pattern speeds at a given simulation time. However, they actually rotate as fast as their spontaneous counterparts in the same galaxy when bar strength is considered, as evidenced by their similar distributions in the pattern speed–bar strength ($\Omega_p - A_2$) space. This highlights that the different evolutionary stages of a bar—given its deceleration—can complicate a direct comparison of pattern speeds at fixed times. For the same reason, we compare the $\Omega_p - A_2$ space across models with different bulge properties. This approach allows us to understand how the bulge influences the pattern speed at a fixed bar strength, thereby accounting for the fact that the bulge delays the bar’s evolutionary stage.

The procedure for tracking bar evolution in the $\Omega_p - A_2$ space is illustrated in Section 3.2 of Paper I; see their Figure 5 for a representative example. In short, we select the A_2 and Ω_p data from both the bar formation and secular growth stages. Within each stage, the data are binned by A_2 , and we compute the median along with the 16th and 84th percentiles of Ω_p in each bin. A key modification from Paper I is that we smooth the A_2 and Ω_p data with a moving average before binning, further mitigating the influence of transient fluctuations on the derived percentiles.

Distributions in the $\Omega_p - A_2$ space for the cold series models are shown in the top row of Figure 3. In the bar formation phase, models with more massive or compact bulges produce bars that start with a higher initial Ω_p and decelerate more rapidly as A_2 increases, reproducing the trends seen in Figure 2. Since this comparison is made at fixed bar strength, it demonstrates that the differences in Ω_p are intrinsic properties linked to the bulge, not merely a consequence of the different evolutionary stages of bars at a given simulation time. Interestingly, all bars converge to a comparable pattern speed by the end of the formation stage, despite attaining different maximum bar strengths. During the secular growth stage, bars in models with a stronger bulge continue to decelerate faster. Consequently, at a given bar strength, they have a lower Ω_p than bars in models with a less massive or less compact bulge.

A reasonable concern is that the bulge’s contribution could “dilute” the measured bar strength, especially during the secular stage when the bar is near saturation. Our Fourier analysis shows that the classical bulge saturates at a maximum $m = 2$ amplitude of ~ 0.10 – 0.15 , significantly lower than the typical bar strength in our simulations. Therefore, according to Equation 4 and 5, a more dominant bulge would indeed yield a lower A_2

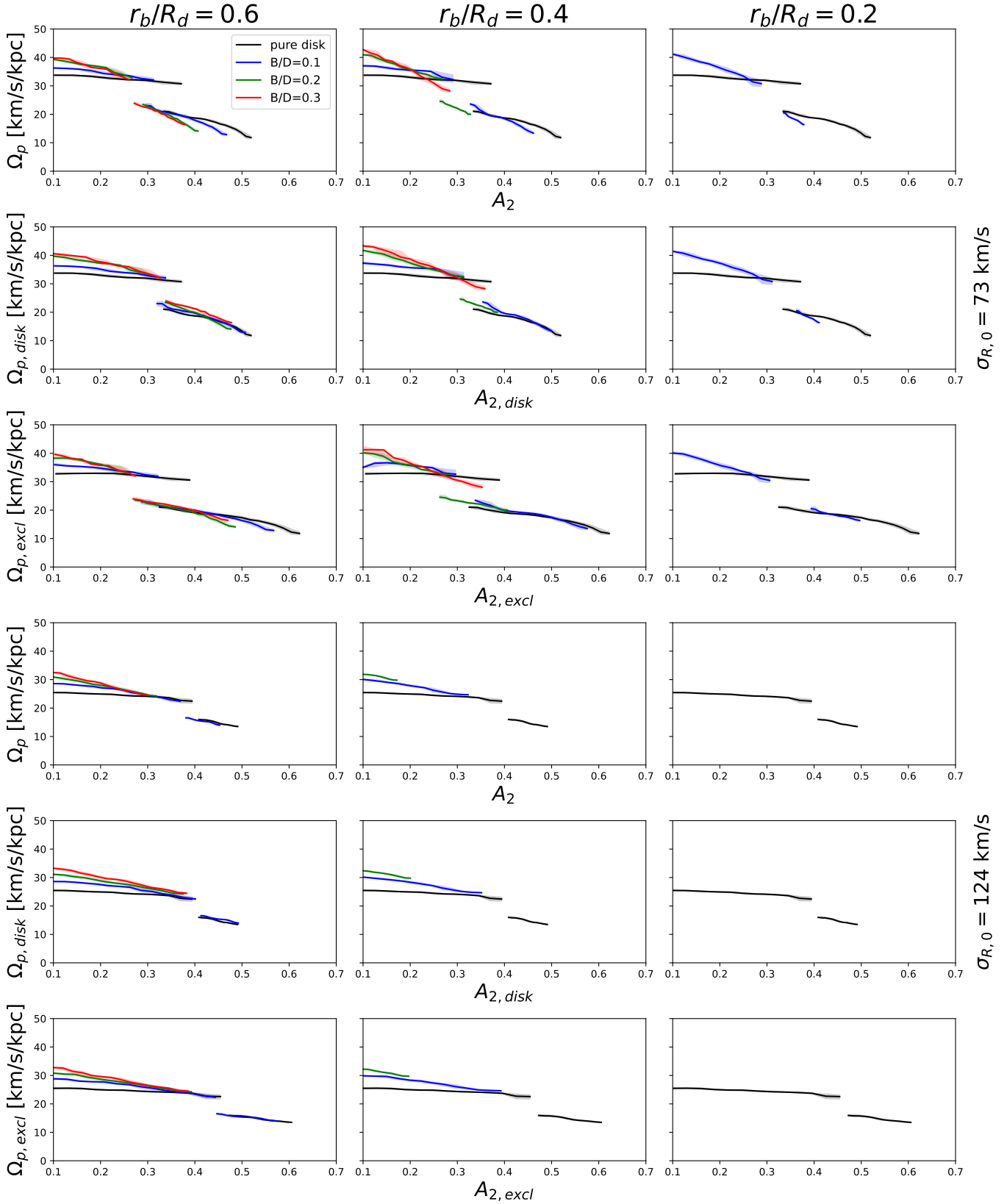


Figure 3. The $\Omega_p - A_2$ space of all simulations. Panel layout and color scheme follow Figure 2. Three definitions of bar strength A_2 are employed: (1) A_2 from all stars within $4 R_d$ (rows 1 & 4); (2) $A_{2,disk}$ from disk particles only within $4 R_d$, removing the bulge (rows 2 & 5); (3) $A_{2,excl}$ from all stellar particles within $4 R_d$ but excluding the central $1 R_d$, mitigating bulge influence (rows 3 & 6). In the bar formation phase, higher bulge mass leads to higher Ω_p at fixed bar strength. In the secular growth stage, models converge to similar Ω_p at fixed A_2 when the bulge contribution is excluded or reduced.

when the stellar disk has a similar level of distortion. To assess whether bulge-induced dilution of A_2 artificially steepens the Ω_p gradient, we recompute the bar strength and pattern speed using only disk particles. These quantities, labeled $A_{2,\text{disk}}$ and $\Omega_{p,\text{disk}}$, are used to regenerate the $\Omega_p - A_2$ space, shown in the second row of Figure 3.

Even with disk-only measurements, a more massive/compact bulge still leads to a higher initial Ω_p and faster deceleration at fixed A_2 during the bar formation stage. Strikingly, during the secular growth stage, the pattern speeds across models converge to similar values at fixed A_2 , which is not previously observed. These results imply that the bulge exerts a stronger influence on the pattern speed during bar formation, whereas in the secular stage, the evolution of Ω_p is largely governed by the disk component, with the direct influence of the bulge possibly becoming less dominant.

In real observations, the clean separation of the disk and bulge components could be challenging. Therefore, we introduce an alternative, more practical method to reduce the bulge’s effect on the measured bar strength. We simply exclude all particles within the central $1 R_d$ when calculating the $m = 2$ Fourier amplitudes, obtaining $A_{2,\text{excl}}$ and $\Omega_{p,\text{excl}}$ (shown in the third row of Figure 3). The resulting $\Omega_p - A_2$ distributions closely match those derived from disk-only particles, deviating only slightly during the final saturation phase. This consistency reinforces the conclusion that the disk component governs pattern speed evolution in the secular stage.

The bottom three rows of Figure 3 display the $\Omega_p - A_2$ distributions for the warm model series. Despite the fact that most bars in the warm models do not have a secular evolution phase, their behavior in the $\Omega_p - A_2$ space is qualitatively similar to that of the cold series.

3.3. $\Delta L_z - A_2$ space

Our earlier analysis attributed the similar pattern speeds at fixed A_2 of bars formed under different mechanisms to the consistent angular momentum loss in the inner disk, as illustrated in Figure 7 of Paper I. Guided by this physical picture, we now examine the angular momentum loss–bar strength ($\Delta L_z - A_2$) space. Here, ΔL_z is defined as the angular momentum loss of the stellar components within $4R_d$, i.e., the change relative to its initial value:

$$\Delta L_z = L_z(< 4 R_d) - L_{z,\text{ini}}(< 4 R_d). \quad (8)$$

Using the same reduction procedure as in the $\Omega_p - A_2$ analysis, we plot the distribution of bars in the $\Delta L_z - A_2$ space.

The first row of Figure 4 shows that all cold-series models lose the same amount of angular momentum at

the onset of bar formation. However, models with more massive or compact bulges start with greater angular momentum, as indicated by their higher circular speeds (Figure 1). Consequently, these models retain a higher residual angular momentum after this initial loss, which translates into a higher pattern speed in the early bar formation stage. These models then exhibit a faster loss of angular momentum as their bar grows stronger, explaining the faster deceleration in pattern speed at fixed bar strength seen in the $\Omega_p - A_2$ space. This enhanced loss persists throughout the secular stage, resulting in a lower final pattern speed for bars in models with more massive/compact bulges. The consistency between the $\Omega_p - A_2$ and $\Delta L_z - A_2$ spaces supports our proposal that the difference in pattern speed at fixed bar strength stems from differing amounts of angular momentum loss of stars.

Analogous to the $\Omega_p - A_2$ space analysis, we also plot the $\Delta L_z - A_2$ space using disk-only measurements (second row of Figure 4) and measurements that exclude the central $1 R_d$ (third row of Figure 4) to mitigate the bulge’s influence. For these cases, the angular momentum loss ΔL_z is computed using only disk particles or by excluding particles within the central $1 R_d$, respectively.

The $\Omega_p - A_2$ and $\Delta L_z - A_2$ spaces present a consistent picture: once bulge contributions are minimized, models exhibit similar angular momentum loss ΔL_z at fixed A_2 during secular evolution, just as they show similar pattern speeds Ω_p . As a further check, we examined hybrid spaces where ΔL_z includes the bulge but A_2 is measured from the disk only ($A_{2,\text{disk}}$) or with the center excluded ($A_{2,\text{excl}}$). The key trends in these hybrid spaces are identical to those in the fully bulge-reduced analysis.

The results for the warm model series (bottom three rows of Figure 4) further reinforce the consistency between the $\Omega_p - A_2$ and $\Delta L_z - A_2$ spaces.

Our results provide a kinematic insight for understanding the bulge’s influence on bar pattern speed. The bulge increases the initial angular momentum of the inner stellar disk, leading to a higher pattern speed during the bar formation stage. It also promotes a greater loss of angular momentum at a fixed growth of bar strength. Although the bulge itself gains angular momentum during its co-evolution with the bar, we find that the amount gained by the bulge is significantly smaller than the amount lost by the inner stellar disk, consistent with previous studies (Saha et al. 2016; Kataria & Das 2018). We suggest that the presence of bulge components enhances the transfer of angular momentum from the inner stellar disk to the outer disk and halo within the same growth in bar strength, re-

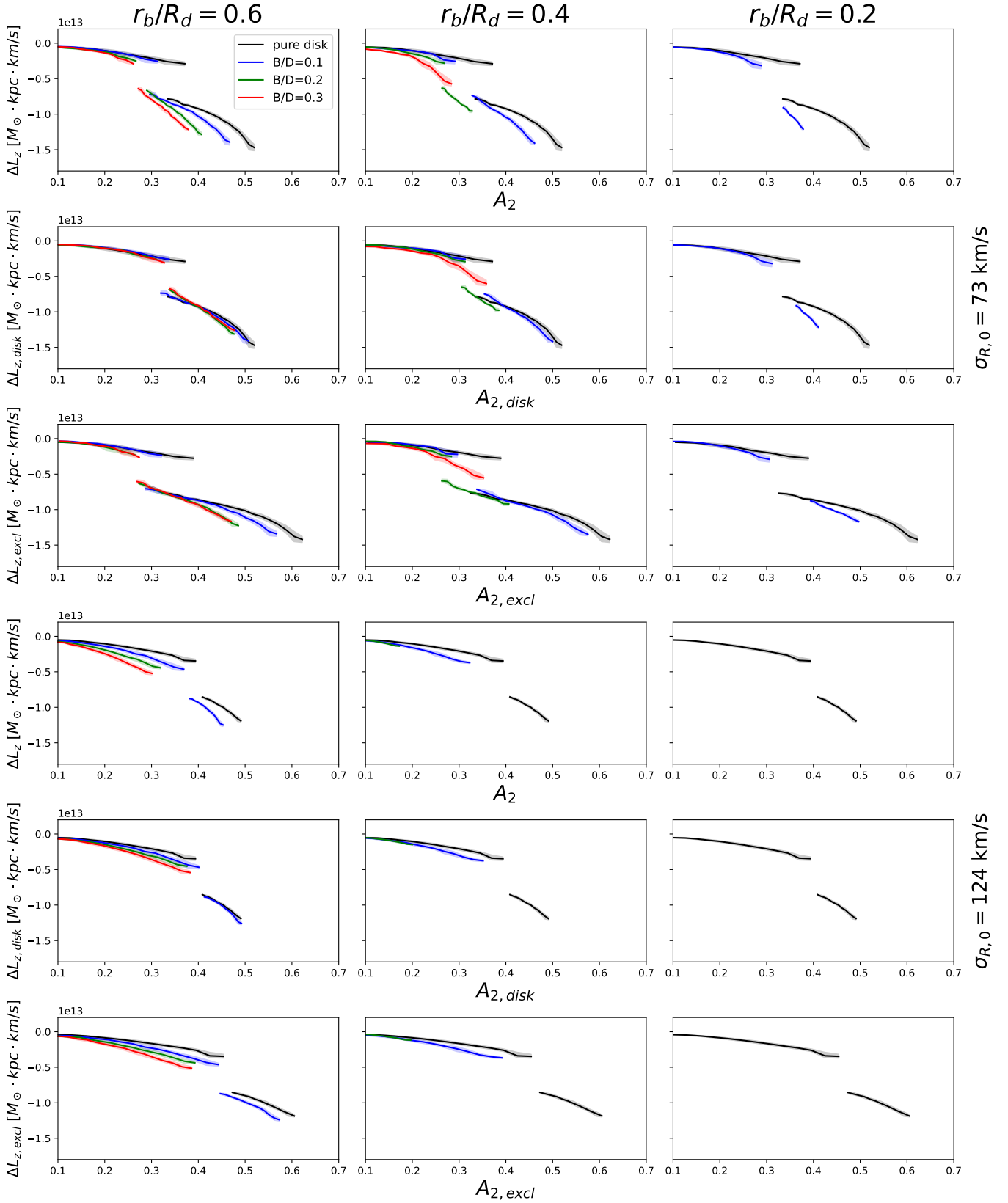


Figure 4. Similar to Figure 3, but in the $\Delta L_z - A_2$ space. The y -axis shows the change in angular momentum (ΔL_z) of the stellar disk within $4 R_d$. During bar formation, stronger bulges lead to greater angular momentum loss in the disk at a given bar strength. In the secular growth stage, however, models exhibit comparable ΔL_z at fixed A_2 once the bulge's contribution is removed or reduced.

sulting in faster pattern speed deceleration rate. During the secular growth stage, the disk component dominates the evolution of both angular momentum and pattern speed, whereas the bulge’s influence may become less important.

3.4. \mathcal{R} ratio

To further investigate how the bulge affects bar pattern speed, we analyze the co-rotation to bar-length ratio, defined as $\mathcal{R} = R_{\text{CR}}/R_{\text{bar}}$ (Debattista & Sellwood 1998, 2000). Bars with $\mathcal{R} < 1.4$ are considered “fast”, and those with $\mathcal{R} > 1.4$ are “slow”. Measurements of R_{CR} and R_{bar} follow the methods detailed in Paper I (Section 3.4 and Appendix). Briefly, R_{CR} is the radius where the bar pattern speed equals the local circular frequency ($\Omega_p = \Omega_c(R_{\text{CR}})$). The bar length R_{bar} is identified as the radius where the $m = 2$ phase angle deviates from the bar’s near-constant value by 5° . We apply a 0.2 Gyr moving average to both R_{CR} and R_{bar} to reduce fluctuations.

The evolution of the co-rotation radius R_{CR} , bar length R_{bar} , and their ratio \mathcal{R} are shown in Figure 5. To compare the evolution meaningfully despite varying bar formation times, we plot them against $t - t_0$, where t_0 is defined as the time when the bar strength A_2 reaches 0.1. In all simulations, the co-rotation radius R_{CR} gradually increases as the bar slows down. Regardless of the bulge properties, bars in all simulations show comparable lengths R_{bar} after formation. This similarity suggests that the bar length is determined primarily by the disk properties—which are common to all models—rather than by the bulge. When the bar buckles, its length drops rapidly, producing a bump in the evolution of \mathcal{R} , since R_{CR} does not change significantly at the same time.

Comparing different simulations, bars in models with a more massive/compact bulge show a smaller \mathcal{R} ratio at the beginning of bar formation, which indicates a faster rotation rate. However, the difference in \mathcal{R} ratio becomes less significant as the bars grow. They reach a similar \mathcal{R} ratio prior to the buckling stage, which is consistent with the similar pattern speed observed at the end of the formation stage in the $\Omega_p - A_2$ space. After the bump caused by the buckling, bars in different models show a comparable \mathcal{R} ratio, which is consistent with the similar pattern speed at fixed bar strength during the secular growth stage when the bulge contribution is removed or reduced (the second/fifth and third/sixth rows of Figure 3). These results further confirm that the bulge’s influence on the bar pattern speed is more significant during the bar formation stage, while in the secular growth stage, the disk component dominates the

pattern speed evolution, and the bulge may only have a limited impact.

4. BULGE EFFECTS ON BAR GROWTH TIMESCALE

Following Bland-Hawthorn et al. (2023), we quantify the bar growth timescale by fitting an exponential function to the A_2 growth during the bar formation stage. The function is defined as:

$$A_2(t) = 0.1 \exp((t - t_0)/\tau_{\text{bar}}), \quad (9)$$

where t_0 (the time when $A_2 = 0.1$) marks the bar onset, and τ_{bar} quantifies the growth timescale. Paper II demonstrated that different exponential fitting forms produce consistent τ_{bar} values with variations of approximately 20% while keeping comparable goodness-of-fit. Consequently, we treat 20% as an acceptable uncertainty for τ_{bar} . Full details of the fitting methodology and its validation are given in Section 3 and the Appendix of Paper II.

The fitting results are presented in Figure 6, with the fitted parameters noted in each panel’s text box where applicable. Most simulations display an exponential growth in bar strength, and the fitted curves capture the A_2 evolution accurately. This behavior aligns with the prediction by the swing amplification feedback loop.

We then compare the fitted parameters in Figure 7. The left column shows the fitted onset times t_0 . A more massive bulge delays bar formation, yielding a larger t_0 . Similarly, for a fixed bulge mass, a more compact bulge also delays the onset. This is consistent with the stronger stabilizing effect that a more massive or compact bulge exerts on the inner stellar disk, as reflected in the higher Toomre Q profiles shown in Figure 1.

The middle left column displays the fitted growth timescale τ_{bar} . According to the Fujii relation (Fujii et al. 2018; Bland-Hawthorn et al. 2023), the bar growth timescale is sensitive to f_{disk} , the disk mass fraction. Since a more massive bulge reduces f_{disk} , it should—and indeed does—produce a longer τ_{bar} , indicating slower bar growth. A more compact bulge likewise tends to increase τ_{bar} , with a few exceptions¹.

Based on *pure disk models*, Chen & Shen (2025) proposed an empirical relation to predict the bar growth timescale using the disk mass fraction ($f_{\text{disk}}(2.2R_d)$), Toomre $Q(2.2R_d)$, and the disk scale height (h_z):

$$\frac{\tau_{\text{bar,pred}}}{C} = Q(2.2 R_d) \frac{h_z}{R_d} \exp\left(-\frac{f_{\text{disk}}(2.2 R_d)}{0.110}\right), \quad (10)$$

¹ Specifically, the cold model with $B/D = 0.1$, $r_b/R_d = 0.2$ and the warm model with $B/D = 0.2$, $r_b/R_d = 0.4$.

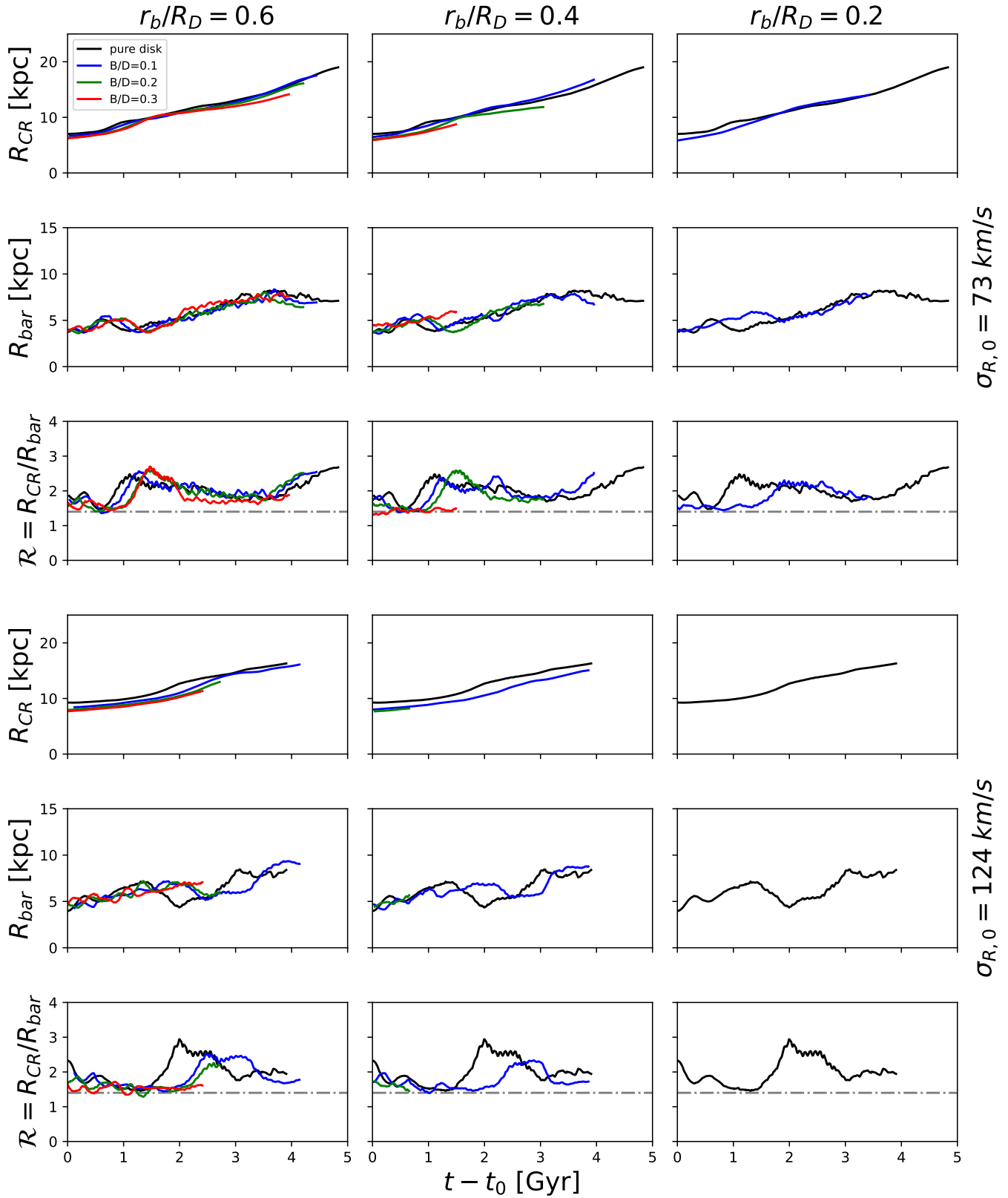


Figure 5. Time evolution of the co-rotation to bar-length ratio (denoted \mathcal{R}) since bar formation (t_0 , defined at $A_2=0.1$). Layout and coloring match Figure 2. The vertical axis displays R_{CR} , R_{bar} , and their ratio \mathcal{R} . The horizontal dash-dotted line indicates $\mathcal{R} = 1.4$, separating fast and slow bars. Reliable measurement of R_{CR} becomes impossible beyond $\sim 10 R_d$ due to low particle counts; these epochs are omitted. Bars in models with a more massive bulge show a lower \mathcal{R} ratio at their birth but hold a similar \mathcal{R} ratio after buckling.

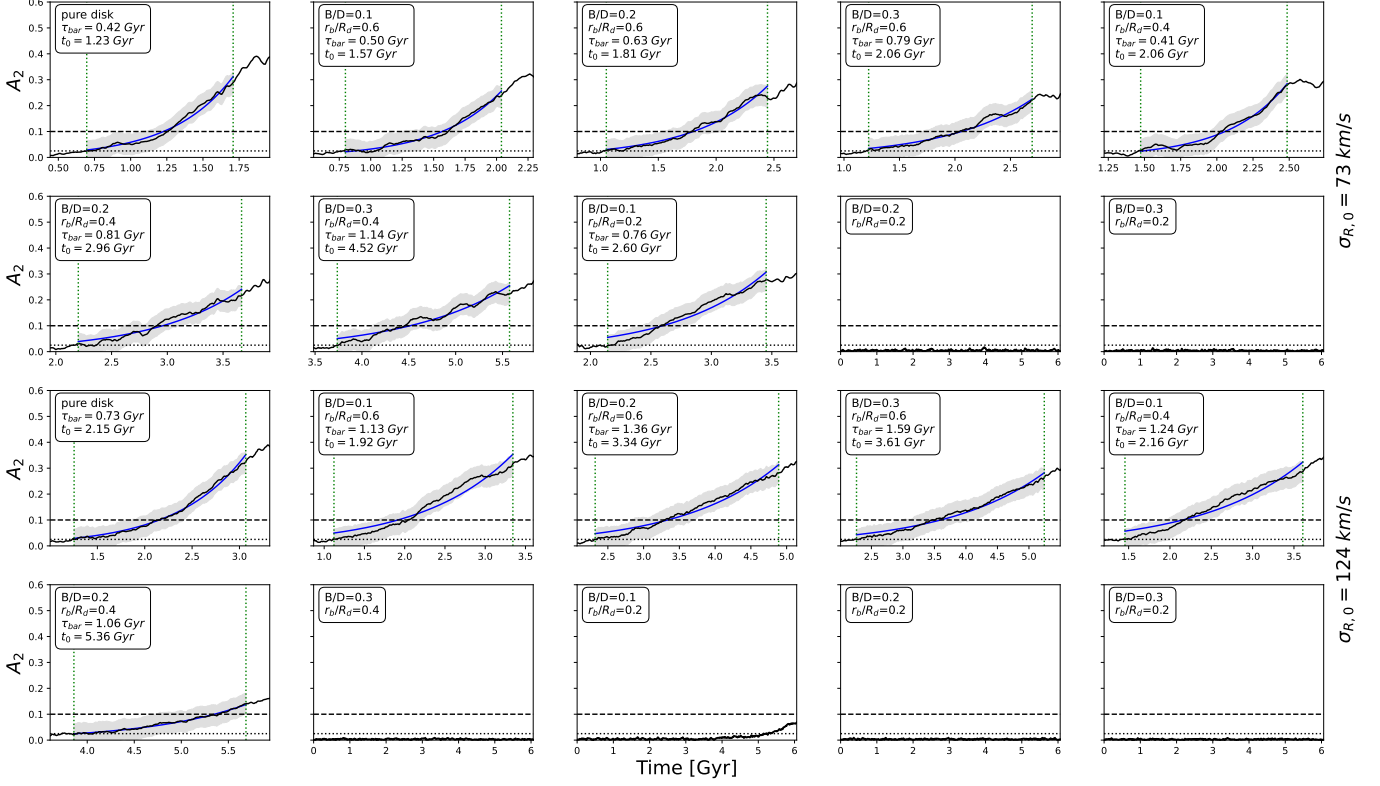


Figure 6. Exponential fitting to the A_2 growth. The evolution of A_2 is shown by the black solid line, with its 1σ spread indicated by the gray shading. The blue solid line represents the exponential fit. The regions used for fitting are denoted by green vertical dotted lines. The text box notes the model information of bulge-to-disk mass fraction ($B/D = 0.1, 0.2,$ and 0.3), the bulge scale radius to the stellar disk scale length ratio ($r_b/R_d = 0.6, 0.4,$ and 0.2). When applicable, the fitted parameters for the bar growth timescale (τ_{bar}) and onset time (t_0) are also provided.

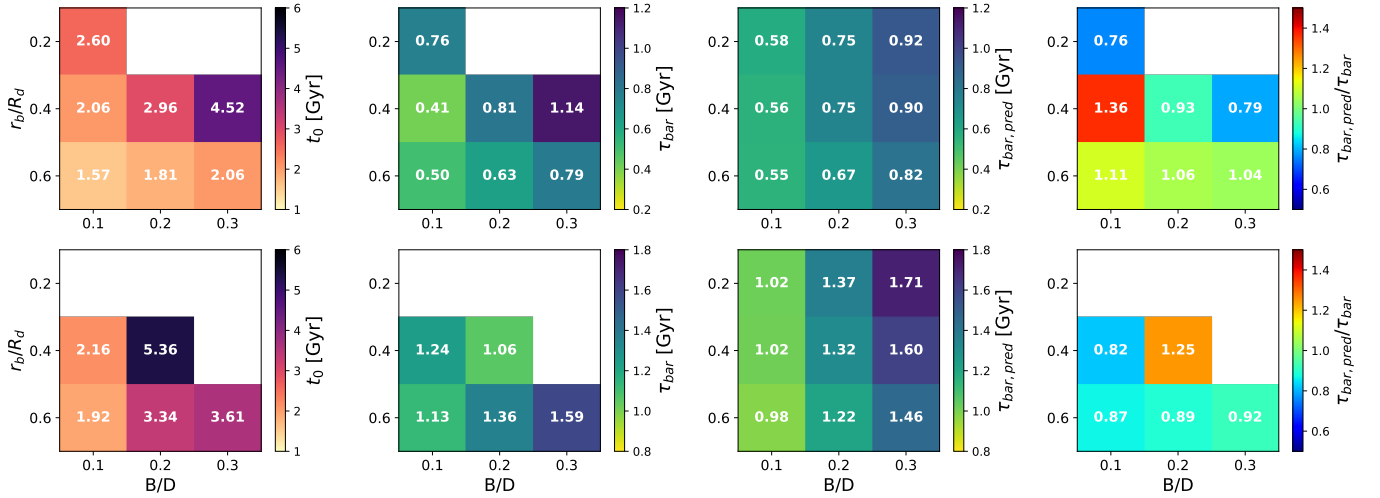


Figure 7. Results of the exponential fitting for the cold series (top row) and warm series (bottom row). **Left column:** fitted onset time t_0 (when A_2 reaches 0.1). More massive/compact bulges delay bar formation, yielding a larger t_0 . **Middle left column:** fitted growth timescale τ_{bar} . More massive/compact bulges slow bar growth, leading to larger τ_{bar} . **Middle right column:** predicted growth timescale $\tau_{\text{bar,pred}}$ based on Chen & Shen (2025). **Right column:** ratio of the predicted to fitted timescale, $\tau_{\text{bar,pred}}/\tau_{\text{bar}}$.

We apply this relation to our galaxies with bulges to predict $\tau_{\text{bar,pred}}$ and compare it with the fitted τ_{bar} values. This comparison aims to identify potential directions for improving the prediction of bar growth timescales in galaxies with bulges.

The right-hand side of Equation 10 is dimensionless and irrelevant to the simulation scaling. Therefore, it does not set the physical time unit; the parameter C must be calibrated to match our simulation scaling. We calibrate C using the fitted τ_{bar} value and the relevant parameters of the isolated pure disk model in the cold series, obtaining $C = 375 \text{ Gyr}$.² With this calibrated C , we compute the predicted bar growth timescale for our models containing a bulge via Equation 10 and compare it with the fitted τ_{bar} values (the middle-right and right columns of Figure 7).

The predicted growth timescale shows reasonable agreement with the fitted τ_{bar} values (within the $\sim 20\%$ uncertainty) for models with diffuse bulges ($r_b/R_d = 0.6$). Moreover, the relation correctly reproduces the trend of longer τ_{bar} for more massive bulges. This agreement implies that the formula of Chen & Shen (2025)—via its influence on $f_{\text{disk}}(2.2R_d)$ —may already effectively account for the effect of bulge mass on the bar growth rate.

A key limitation of Equation 10 is its inability to account for bulge compactness: it yields similar predicted $\tau_{\text{bar,pred}}$ values for models sharing the same bulge mass but different r_b/R_d . This shortcoming is starkly evident in highly compact bulges that completely suppress bar formation within 6 Gyr, implying a much longer true growth timescale than predicted. The root cause is that both $Q(2.2R_d)$ and $f_{\text{disk}}(2.2R_d)$ —the formula’s inputs—are nearly identical for such models (see Figure 1), rendering them insensitive to compactness. This indicates that either (1) we should measure Q and f_{disk} at a smaller radius, where compactness has a stronger effect, or (2) a compactness parameter should be added explicitly to the formula.

A more definitive assessment of how bulge compactness affects the bar growth timescale would require a larger suite of simulations and a more systematic analysis, which is beyond the scope of the present study and will be pursued in future work.

5. SUMMARY

We conduct a suite of controlled N -body simulations to examine the effect of classical bulges on spontaneous bar formation and subsequent bar properties. We gen-

erate a series of galaxy models with bulges spanning a range of bulge-to-disk mass ratios and compactness. A more massive or compact bulge increases the Toomre Q parameter and reduces the disk mass fraction (f_{disk}) in the central region (Figure 1).

We evolve these galaxy models in isolation and measure the resulting bar strength and pattern speed (Figure 2). A more massive or compact bulge delays bar formation and seems to produce a higher pattern speed. If the bulge is sufficiently massive and compact, bar formation is completely suppressed within the 6 Gyr simulation timeframe.

To facilitate a fair comparison of bar pattern speeds, we construct the pattern speed–bar strength ($\Omega_p - A_2$) space, which accounts for differences in evolutionary stage (Figure 3). In the early formation stage, bars in models with more massive or compact bulges have a higher initial pattern speed Ω_p but decelerate more rapidly as the bar strengthens. This accelerated deceleration persists into the secular growth stage, leading to a lower Ω_p at a fixed bar strength. After removing or reducing the bulge’s “diluting” effect on the measured bar strength, the same trends—higher initial Ω_p and faster deceleration—persist in the bar formation stage. However, the pattern speeds become similar in the secular stage. These results indicate that the bulge strongly influences the pattern speed during bar formation, but its role may become less important in the secular stage, where the disk component dominates the evolution of Ω_p .

A kinematic insight of these results is provided in the angular momentum loss–bar strength ($\Delta L_z - A_2$) space (Figure 4). A more massive or compact bulge increases the initial angular momentum of the inner disk, leading to a higher initial pattern speed. The bulge promotes the transfer of angular momentum from the inner stellar disk to the outer regions and the halo, driving a faster deceleration in pattern speed. During the secular growth stage, the disk component dominates the angular momentum evolution and consequently the evolution of the pattern speed.

The trend in pattern speed evolution is also reflected by the \mathcal{R} ratio (Figure 5). Bars in models with more massive/compact bulges have a smaller \mathcal{R} at the early stage of bar formation, but the difference in \mathcal{R} becomes smaller during the growth of the bar and eventually becomes indistinguishable in the secular growth stage. These results echo the conclusion from the $\Omega_p - A_2$ space that the bulge’s effect on the pattern speed is more significant during the formation stage but can be less important in the secular growth stage.

² Calibrating with the warm pure disk model yields a slightly different C but does not alter our conclusions.

We quantify the bar growth by applying an exponential fit to the A_2 evolution to measure the onset time t_0 and the growth timescale τ_{bar} (Figure 6). More massive or compact bulges delay bar formation (larger t_0), and the bars in these models grow more slowly, as reflected in their larger τ_{bar} .

This paper investigates the effect of classical bulges on bar formation and properties under the internal formation mechanism. To build a more complete picture, the subsequent study (Paper IIIB) will explore the role of bulges in tidally induced bar formation. The combined analysis of both internal and external formation scenarios will allow for a direct comparison of how bulge properties influence bars under these distinct mechanisms.

Software: AGAMA (Vasiliev 2019), GADGET-4 (Springel 2005; Springel et al. 2021). NumPy (Harris

et al. 2020), SciPy (Virtanen et al. 2020), Matplotlib (Hunter 2007), Jupyter Notebook (Kluyver et al. 2016)

ACKNOWLEDGEMENTS

We thank Thor Tepper-Garcia and Joss Bland-Hawthorn for their help with the AGAMA work and with initializing the galaxy models. We thank Xufen Wu, Zhi Li, and Sandeep Kumar Kataria for their valuable insights on simulations and analysis. We also thank Rui Guo for their helpful discussions. The research presented here is partially supported by the National Natural Science Foundation of China under grant Nos. 12533004, 12025302, 11773052; by China Manned Space Program with grant no. CMS-CSST-2025-A11; and by the “111” Project of the Ministry of Education of China under grant No. B20019. This work made use of the Gravity Supercomputer at the Department of Astronomy, Shanghai Jiao Tong University.

REFERENCES

- Athanassoula, E. 2003, MNRAS, 341, 1179, doi: [10.1046/j.1365-8711.2003.06473.x](https://doi.org/10.1046/j.1365-8711.2003.06473.x)
- Binney, J. 2020, MNRAS, 496, 767, doi: [10.1093/mnras/staa1485](https://doi.org/10.1093/mnras/staa1485)
- Binney, J., & Tremaine, S. 2008, Galactic Dynamics: Second Edition
- Bland-Hawthorn, J., Tepper-Garcia, T., Agertz, O., & Federrath, C. 2024, ApJ, 968, 86, doi: [10.3847/1538-4357/ad4118](https://doi.org/10.3847/1538-4357/ad4118)
- Bland-Hawthorn, J., Tepper-Garcia, T., Agertz, O., & Freeman, K. 2023, ApJ, 947, 80, doi: [10.3847/1538-4357/acc469](https://doi.org/10.3847/1538-4357/acc469)
- Bland-Hawthorn, J., Tepper-Garcia, T., Agertz, O., et al. 2025, arXiv e-prints, arXiv:2502.01895, doi: [10.48550/arXiv.2502.01895](https://doi.org/10.48550/arXiv.2502.01895)
- Byrd, G. G., Valtonen, M. J., Sundelius, B., & Valtaoja, L. 1986, A&A, 166, 75
- Chen, B.-H., & Shen, J. 2025, ApJ, 990, 140, doi: [10.3847/1538-4357/adf966](https://doi.org/10.3847/1538-4357/adf966)
- Debattista, V. P., & Sellwood, J. A. 1998, ApJL, 493, L5, doi: [10.1086/311118](https://doi.org/10.1086/311118)
- . 2000, ApJ, 543, 704, doi: [10.1086/317148](https://doi.org/10.1086/317148)
- Dubinski, J., Berentzen, I., & Shlosman, I. 2009, ApJ, 697, 293, doi: [10.1088/0004-637X/697/1/293](https://doi.org/10.1088/0004-637X/697/1/293)
- Erwin, P. 2018, MNRAS, 474, 5372, doi: [10.1093/mnras/stx3117](https://doi.org/10.1093/mnras/stx3117)
- Fujii, M. S., Bédorf, J., Baba, J., & Portegies Zwart, S. 2018, MNRAS, 477, 1451, doi: [10.1093/mnras/sty711](https://doi.org/10.1093/mnras/sty711)
- Gauthier, J.-R., Dubinski, J., & Widrow, L. M. 2006, ApJ, 653, 1180
- Ghosh, S., Fragkoudi, F., Di Matteo, P., & Saha, K. 2023, A&A, 674, A128, doi: [10.1051/0004-6361/202245275](https://doi.org/10.1051/0004-6361/202245275)
- Goldreich, P., & Lynden-Bell, D. 1965, MNRAS, 130, 125, doi: [10.1093/mnras/130.2.125](https://doi.org/10.1093/mnras/130.2.125)
- Guo, Y., Jogee, S., Wise, E., et al. 2024, arXiv e-prints, arXiv:2409.06100, doi: [10.48550/arXiv.2409.06100](https://doi.org/10.48550/arXiv.2409.06100)
- Harris, C. R., Millman, K. J., van der Walt, S. J., et al. 2020, Nature, 585, 357–362, doi: [10.1038/s41586-020-2649-2](https://doi.org/10.1038/s41586-020-2649-2)
- Hernquist, L. 1990, ApJ, 356, 359
- Hohl, F. 1971, ApJ, 168, 343
- Hozumi, S. 2022, MNRAS, 510, 4394, doi: [10.1093/mnras/stab3704](https://doi.org/10.1093/mnras/stab3704)
- Hunter, J. D. 2007, Computing in Science Engineering, 9, 90, doi: [10.1109/MCSE.2007.55](https://doi.org/10.1109/MCSE.2007.55)
- Iles, E. J., Pettitt, A. R., & Okamoto, T. 2022, MNRAS, 510, 3899, doi: [10.1093/mnras/stab3330](https://doi.org/10.1093/mnras/stab3330)
- Jang, D., & Kim, W.-T. 2023, ApJ, 942, 106, doi: [10.3847/1538-4357/aca7bc](https://doi.org/10.3847/1538-4357/aca7bc)
- Julian, W. H., & Toomre, A. 1966, ApJ, 146, 810, doi: [10.1086/148957](https://doi.org/10.1086/148957)
- Kataria, S. K., & Das, M. 2018, MNRAS, 475, 1653, doi: [10.1093/mnras/stx3279](https://doi.org/10.1093/mnras/stx3279)
- Kluyver, T., Ragan-Kelley, B., Pérez, F., et al. 2016, in Positioning and Power in Academic Publishing: Players, Agents and Agendas, ed. F. Loizides & B. Schmidt, IOS Press, 87 – 90
- Le Conte, Z. A., Gadotti, D. A., Ferreira, L., et al. 2024, MNRAS, 530, 1984, doi: [10.1093/mnras/stae921](https://doi.org/10.1093/mnras/stae921)

- Lee, Y. H., Ann, H. B., & Park, M.-G. 2019, *ApJ*, 872, 97, doi: [10.3847/1538-4357/ab0024](https://doi.org/10.3847/1538-4357/ab0024)
- Li, Z., Shen, J., & Kim, W.-T. 2015, *ApJ*, 806, 150, doi: [10.1088/0004-637X/806/2/150](https://doi.org/10.1088/0004-637X/806/2/150)
- Lin, L., Li, C., He, Y., Xiao, T., & Wang, E. 2017, *ApJ*, 838, 105, doi: [10.3847/1538-4357/aa657a](https://doi.org/10.3847/1538-4357/aa657a)
- Lin, L., Li, C., Du, C., et al. 2020, *MNRAS*, 499, 1406, doi: [10.1093/mnras/staa2913](https://doi.org/10.1093/mnras/staa2913)
- Łokas, E. L. 2019a, *A&A*, 629, A52, doi: [10.1051/0004-6361/201936056](https://doi.org/10.1051/0004-6361/201936056)
- . 2019b, *A&A*, 624, A37, doi: [10.1051/0004-6361/201935011](https://doi.org/10.1051/0004-6361/201935011)
- Łokas, E. L., Ebrova, I., del Pino, A., et al. 2016, *ApJ*, 826, 227, doi: [10.3847/0004-637X/826/2/227](https://doi.org/10.3847/0004-637X/826/2/227)
- Marinova, I., & Jogee, S. 2007, *ApJ*, 659, 1176, doi: [10.1086/512355](https://doi.org/10.1086/512355)
- Martinez-Valpuesta, I., Aguerri, J. A. L., Gonzalez-Garca, A. C., Dalla Vecchia, C., & Stringer, M. 2017, *MNRAS*, 464, 1502, doi: [10.1093/mnras/stw2500](https://doi.org/10.1093/mnras/stw2500)
- Masters, K. L., Nichol, R. C., Hoyle, B., et al. 2011, *MNRAS*, 411, 2026
- McClure, R. L., Geron, T., D’Onghia, E., et al. 2025, arXiv e-prints, arXiv:2506.09150, doi: [10.48550/arXiv.2506.09150](https://doi.org/10.48550/arXiv.2506.09150)
- Menendez-Delmestre, K., Sheth, K., Schinnerer, E., Jarrett, T. H., & Scoville, N. Z. 2007, *ApJ*, 657, 790, doi: [10.1086/511025](https://doi.org/10.1086/511025)
- Ostriker, J. P., & Peebles, P. J. 1973, *ApJ*, 186, 467
- Saha, K., & Elmegreen, B. 2018, *ApJ*, 858, 24, doi: [10.3847/1538-4357/aabacd](https://doi.org/10.3847/1538-4357/aabacd)
- Saha, K., Gerhard, O., & Martinez-Valpuesta, I. 2016, *A&A*, 588, A42, doi: [10.1051/0004-6361/201527566](https://doi.org/10.1051/0004-6361/201527566)
- Sellwood, J. 2014, *Reviews of Modern Physics*, 86, 1
- Springel, V. 2005, *MNRAS*, 364, 1105, doi: [10.1111/j.1365-2966.2005.09655.x](https://doi.org/10.1111/j.1365-2966.2005.09655.x)
- Springel, V., Pakmor, R., Zier, O., & Reinecke, M. 2021, *MNRAS*, 506, 2871, doi: [10.1093/mnras/stab1855](https://doi.org/10.1093/mnras/stab1855)
- Toomre, A. 1981, in *Structure and Evolution of Normal Galaxies*, ed. S. M. Fall & D. Lynden-Bell, 111–136
- Vasiliev, E. 2019, *MNRAS*, 482, 1525, doi: [10.1093/mnras/sty2672](https://doi.org/10.1093/mnras/sty2672)
- Virtanen, P., Gommers, R., Oliphant, T. E., et al. 2020, *Nature Methods*, 17, 261, doi: [10.1038/s41592-019-0686-2](https://doi.org/10.1038/s41592-019-0686-2)
- Weinberg, M. D. 1985, *MNRAS*, 213, 451, doi: [10.1093/mnras/213.3.451](https://doi.org/10.1093/mnras/213.3.451)
- Worrakitpoonpon, T. 2025, *ApJ*, 979, 166, doi: [10.3847/1538-4357/ada35f](https://doi.org/10.3847/1538-4357/ada35f)
- Zheng, Y., & Shen, J. 2025, *ApJ*, 979, 60, doi: [10.3847/1538-4357/ad9bae](https://doi.org/10.3847/1538-4357/ad9bae)
- Zheng, Y., Shen, J., Wu, X., & Chen, B.-H. 2025, *ApJ*, 986, 90, doi: [10.3847/1538-4357/adcf93](https://doi.org/10.3847/1538-4357/adcf93)